Classification and environmental properties of X-ray selected point-like sources in the XMM-LSS field

O. Melnyk, M. Plionis, A. Elyiv, M. Salvato, L. Chiappetti, N. Clerc, P. Gandhi, M. Pierre, T. Sadibekova, A. Pospieszalska-Surdej, et al.

A&A 557, A81 (2013)
DOI: 10.1051/0004-6361/201220624

Astronomy & Astrophysics

Classification and environmental properties of X-ray selected point-like sources in the XMM-LSS field⋆

O. Melnyk[1,2], M. Plionis[3,4], A. Elyiv[1,5], M. Salvato[6,7], L. Chiappetti[8], N. Clerc[6], P. Gandhi[9], M. Pierre[10], T. Sadibekova[10], A. Pospieszalska-Surdej[1], and J. Surdej[1]

[1] Institut d'Astrophysique et de Géophysique, Université de Liège, 4000 Liège, Belgium
e-mail: melnykol@gmail.com
[2] Astronomical Observatory, Taras Shevchenko National University of Kyiv, 3 Observatorna St., 04053 Kyiv, Ukraine
[3] Physics Dept., Aristotle Univ. of Thessaloniki, 54124 Thessaloniki, Greece
[4] Instituto Nacional de Astrófisica, Óptica y Electrónica, 72000 Puebla, Mexico
[5] Main Astronomical Observatory, Academy of Sciences of Ukraine, 27 Akademika Zabolotnoho St., 03680 Kyiv, Ukraine
[6] Max-Planck-Institute for Extraterrestrial Physics, Giessenbachstrasse 1, 85748 Garching, Germany
[7] Excellence Cluster, Boltzmannstrass 2, 85748 Garching, Germany
[8] INAF-IASF Milano, via Bassini 15, 20133 Milano, Italy
[9] Institute of Space and Astronautical Science (ISAS), Japan Aerospace Exploration Agency, 3-1-1 Yoshinodai, Chuo-ku, Sagamihara, 252−5210 Kanagawa, Japan
[10] DSM/Irfu/SAp, CEA/Saclay, 91191 Gif-sur-Yvette Cedex, France

Received 24 October 2012 / Accepted 1 July 2013

ABSTRACT

Context. The XMM-Large Scale Structure survey, covering an area of 11.1 sq. deg., contains more than 6000 X-ray point-like sources detected with the *XMM-Newton* to a flux of 3×10^{-15} erg s^{-1} cm^{-2} in the [0.5−2] keV band. The vast majority of these sources have optical (CFHTLS), infrared (SWIRE IRAC and MIPS), near-infrared (UKIDSS), and/or ultraviolet (GALEX) counterparts.
Aims. We wish to investigate the environmental properties of the different types of the XMM-LSS X-ray sources by defining their environment using the i'-band CFHTLS W1 catalog of optical galaxies to a magnitude limit of 23.5 mag.
Methods. We have classified 4435 X-ray selected sources on the basis of their spectra, SEDs, and X-ray luminosity, and estimated their photometric redshifts, which have a 4−11 band photometry with an accuracy of $\sigma_{\Delta z/(1+z_{sp})} = 0.076$ with 22.6% outliers for $i' < 26$ mag. We estimated the local overdensities of 777 X-ray sources that have spectro-z or photo-z calculated by using more than seven bands (accuracy of $\sigma_{\Delta z/(1+z_{sp})} = 0.061$ with 13.8% outliers) within the volume-limited region defined by $0.1 \le z \le 0.85$ and $-23.5 < M_{i'} < -20$.
Results. Although X-ray sources may be found in variety of environments, a high fraction ($\gtrsim$55−60%), as verified by comparing with the random expectations, reside in overdense regions. The galaxy overdensities within which X-ray sources reside show a positive recent redshift evolution (at least for the range studied; $z \lesssim 0.85$). We also find that X-ray selected galaxies, when compared to AGN, inhabit significantly higher galaxy overdensities, although their spatial extent appear to be smaller than that of AGN. Hard AGN ($HR \ge -0.2$) are located in more overdense regions than soft AGN ($HR < -0.2$), which is clearly seen in both redshift ranges, although it appears to be stronger in the higher redshift range ($0.55 < z < 0.85$). Furthermore, the galaxy overdensities (with $\delta \gtrsim 1.5$) within which soft AGN are embedded appear to evolve more rapidly compared to the corresponding overdensities around hard AGN.

Key words. quasars: general – X-rays: general – galaxies: active – X-rays: galaxies

1. Introduction

Active galactic nuclei (AGN) are among the most powerful energy emitters in the Universe and trace the locations of active supermassive black holes (SMBHs) on the cosmic web. Understanding the nature and evolution of SMBHs as a function of cosmic time and environment constitutes an important goal of modern high-energy astrophysics. In particular the coincidence between the star-formation peak of galaxies at redshifts $z \sim 2-3$ and the corresponding formation peak of high luminosity AGN/QSOs, appears to link the cosmic histories of galaxies and black holes in an intricate way, providing an important input in understanding the formation and evolution of cosmic structures in the Universe (Warren et al. 1994; Schawinski et al. 2009; Fanidakis et al. 2012).

It is known that environmental effects (cf. interactions, minor or major galaxy merging) may affect the physical properties of galaxies, such as their morphological type, color, star-formation rate, nuclear activity, etc. (Dressler 1980; Blanton et al. 2003a; Kauffmann et al. 2004; van der Wel 2008, etc.). The connection between galaxy and black hole formation and evolution indicates that there must be a dependence on the physical properties of AGN and on their triggering mechanism on the environment, which has yet to be clearly established. Important questions are: (a) Is the main determining factor of the galaxy/AGN properties intrinsic evolution or environmental influence? and (b) how do

⋆ Full Table 2 in only available at the CDS via anonymous ftp to cdsarc.u-strasbg.fr (130.79.128.5) or via http://cdsarc.u-strasbg.fr/viz-bin/qcat?J/A+A/557/A81

the host galaxy physical properties and the local environment affect the black hole fuelling mechanisms? To answer these questions, many authors have been studying the properties of AGN environment (density, colors, morphology, etc. of the nearest neighbors) and comparing these properties with those of normal galaxies.

For example, Kauffmann et al. (2004) conclude that both star formation and nuclear activity strongly depend on the environment up to ∼1 Mpc for a fixed stellar mass of galaxies. Waskett et al. (2005) did not find any differences between the environmental properties of AGN and of a control sample of galaxies in the $0.4 < z < 0.6$ redshift range. A qualitatively similar result was obtained by Li et al. (2006), who analyzed the clustering properties of narrow-line AGN. Gilmour et al. (2007) considered the environment of X-ray selected AGN in the supercluster A901/2 (at $z = 0.17$) and found that they prefer dense environments, avoiding the most overdense and underdense regions. Similarly, Lietzen et al. (2009) found that QSOs avoid the densest regions and prefer to reside in the outskirts of superclusters using SDSS data. Constantin et al. (2008) found that local ($z \lesssim 0.09$) AGN are more common in voids than in walls for a same range of masses and accretion rates. The recent analysis of Lietzen et al. (2011) shows that radio-quiet QSOs and Seyfert galaxies prefer low-density regions, in contrast to radio galaxies which prefer more dense environments.

On the basis of X-ray selected AGN in the COSMOS field Silverman et al. (2009) reached the conclusion that AGN prefer to reside in environments that are similar to those of massive galaxies with substantial levels of star formation. The AGN with low stellar mass hosts are located over a wide range of environments but the AGN with high stellar mass hosts prefer low density regions. These results also agree with Montero-Dorta et al. (2009), who found that Seyferts and X-ray selected AGN at $z \sim 1$ almost do not show environmental dependencies. Moreover, low-redshift LINERs and Seyfert galaxies appear to inhabit low density environments contrary to high-redshift LINERs ($z \sim 1$) that favor higher density environments. Contrary to this, Georgakakis et al. (2007; 2008) found that the X-ray population at $z \sim 1$ avoids underdense regions and prefers to reside in groups. Falder et al. (2010) showed that $z \sim 1$ AGN have an excess of galaxy density within a radius of 200−300 kpc and that the local galaxy density increases with the radio AGN luminosity but not with the black hole mass. Bradshaw et al. (2011) showed that X-ray and radio-loud AGN with $1.0 < z < 1.5$ are located in significantly overdense regions with the former being found in the cluster outskirts. Furthermore, recent clustering studies of X-ray selected AGN have shown that they reside in group-size dark matter halos with masses $M_{\rm h} \sim 10^{13}\ h^{-1}\ M_{\odot}$, which are significantly more massive than those inhabited by optical QSOs (see Miyaji et al. 2011; Allevato et al. 2011; Koutoulidis et al. 2013, and references therein).

According to the unified scheme of Antonucci (1993), AGN of different types, like Seyfert type I and II, and broad and narrow line QSOs (unobscured and obscured ones), should inhabit similar environments, since these objects only differ because of the orientation of their torus with respect to the line-of-sight. However, the standard orientation-based AGN unification scheme does not consider any evolution with redshift of the properties of obscured vs. unobscured AGN. Is there some observational evidence establishing a similar environment of the different types of AGN? Statistical studies lead to contradictory results.

Koulouridis et al. (2006) found in the very local Universe that the fraction of Seyfert 2 galaxies with close neighbors is significantly larger than that of their control sample and of Seyfert 1 galaxies, while their large scale environment does not show any difference compared to their control samples (see also Sorrentino et al. 2006 for similar results). At the same time, Strand et al. (2008) have shown that higher luminosity AGN inhabit more overdense environments compared to lower luminosity AGN to 2 Mpc. The authors also found that type II and type I QSOs present similarly overdense environments in the redshift range of $0.3 < z < 0.6$, while the environment of dimmer type I quasars appears to be less overdense than that of type II quasars.

X-ray selected sources, which mainly consist of AGN, offer information about the nature and properties of super massive black holes over a wide redshift range up to $z \sim 4$. Therefore, X-ray surveys combined with a multiwavelength analysis of their host galaxies provide an effective tool for the environmental study of different types of AGN. In our work, we consider the environmental vs. intrinsic properties of X-ray selected point-like sources with optically detected counterparts from the 11.1 sq. deg XMM-Large Scale Structure (LSS) medium-deep extragalactic survey. Earlier versions of our survey over a lower solid angle and a variety of analyses can be found in Chiappetti et al. (2005), Gandhi et al. (2006), Pierre et al. (2007), Tajer et al. (2007), Polletta et al. (2007), Garcet et al. (2007), Tasse et al. (2008a,b) and Nakos et al. (2009).

Regarding previous environmental studies based on the original XMM-LSS field, Tasse et al. (2008b) considered the environment of 110 radio-loud AGN, finding that high and low stellar mass systems are located in different environment. The authors concluded that the AGN triggering mechanism of high mass systems could be produced by cooling of the hot gas and could be explained by the cold gas accretion due to a merging for the low mass systems. In addition, Tasse et al. (2011) found that X-ray selected type 2 AGN show very similar individual and environmental properties to low mass radio-loud AGN.

The main aim of our current work is to consider the environmental properties of different types of X-ray selected XMM-LSS sources using the local density of optical galaxies based on the CFHTLS[1]. In our analysis, we use the newest version of the XMM-LSS multiwavelength catalog (Chiappetti et al. 2012), which contains 6342 X-ray sources[2] over 11.1 sq. deg. The clustering properties of the point-like sources of this catalog were analyzed by Elyiv et al. (2012).

In Sect. 2, we present the XMM-LSS source sample. In Sect. 3, we discuss the classification of the optical counterparts, the photo-z determination technique, and the corresponding results. Section 4 presents the multiwavelength properties of the sources and the samples of the different types of X-ray sources. The results of the environmental analysis are given in Sect. 5. Discussion and general conclusions form Sect. 6. Throughout this work we use the standard cosmology: $\Omega_0 = 0.3$, $\Omega_\Lambda = 0.7$, and $H_0 = 72$ km/s/Mpc.

2. The sample of X-ray sources and their counterparts

The XMM-LSS field occupies an area of 11.1 sq. deg. and is located at high galactic latitudes by [$2^{\rm h}14^{\rm m} < {\rm RA} < 2^{\rm h}30^{\rm m}$; $-6°25^{\rm m} < {\rm Dec} < -2°35^{\rm m}$, J2000.0], as seen in Fig. 1. This field also contains 1.14 sq. deg. the Subaru X-ray Deep Survey

[1] Canada France Hawaii Telescope Legacy Survey: http://www.cfht.hawaii.edu/Science/CFHLS/

[2] In the present paper, we only considered objects from the good fields, where the condition is badfield = 0.

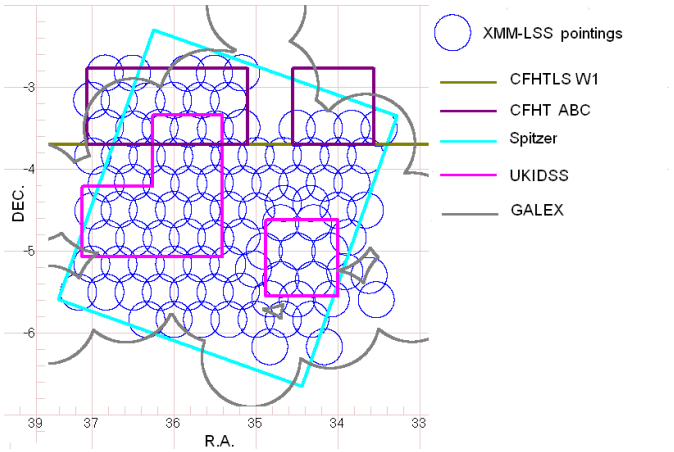

Fig. 1. XMM-LSS field and multiwavelength coverage. CFHT ABC supplementary pointings are not the part of the Legacy Survey.

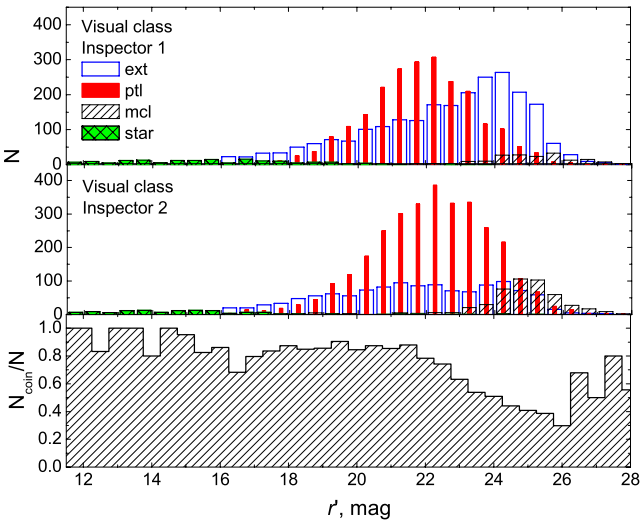

Fig. 2. Magnitude distribution of 5142 visually classified objects by two independent inspectors (the *top and middle panels*). The fractional agreement between the two independent visual classifications is illustrated in the *bottom panel*.

(SXDS) deep field (Ueda et al. 2008). Below we will refer below to the XMM-LSS field as the Full Exposure Field[3], which includes the SXDS field.

The XMM-LSS full exposure field contains 6342 sources[2] detected in the soft (0.5−2 keV) and/or hard (2−10 keV) bands down to a detection likelihood of 15. This corresponds to the following flux limits (50% detection probability): $F_{(0.5-2\ \mathrm{keV})} = 3 \times 10^{-15}$ erg s^{-1} cm^{-2} and $F_{(2-10\ \mathrm{keV})} = 1 \times 10^{-14}$ erg s^{-1} cm^{-2} over nominal survey pointings.

See more details about the catalog sensitivity in Elyiv et al. (2012) and the catalog description paper by Chiappetti et al. (2012). In the latter paper, the details of the soft and hard band merging are also given. From the multiwavelength catalog of the X-ray point-like sources and their counterparts in optical CFHTLS, infrared SWIRE[4]/IRAC[5], infrared MIPS[6], near-infrared UKIDSS[7], and ultraviolet GALEX[8], we only selected those sources that have a counterpart at optical wavelength or more wavelengths. The detailed description of the matching of X-ray sources with their multiwavelength counterparts is given in Chiappetti et al. (2012).

We only took one counterpart for each X-ray source: that which had the best *probXO* probability (see definition below) and a rank of 0 (single counterpart) or 1 (preferred counterpart but there is more than one), see Chiappetti et al. (2012) for details. The total number of X-ray selected sources with corresponding counterparts are 5142.

Each counterpart was visually inspected using CFHTLS g', i', and r' images from the sixth release by two independent inspectors. The majority of the counterparts have g'- and r'-band observations: 5078 sources are visible in the g'-band and 5047 in the r'-band, respectively. According to our rough visual classification, the sources were split into extended sources (*ext*), and point-like sources (*ptl*) with the latter consisting mostly of QSOs and stars. We reserved one more category for very faint/invisible objects, photo-defects, etc. These objects are referred as misclassified objects (*mcl*). The top and middle panels of Fig. 2 show the distribution of sources as a function of their apparent r' magnitude, according to the two independent inspectors. The second inspector tends to classify faint objects and objects with bright nuclei as *ptl*, while the first inspector classifies most of these objects as *ext*. Similar types were assigned by both inspectors for about 90% of the objects up to ∼22 mag (see the bottom panel of Fig. 2).

Therefore, we preliminary considered 2441 optical counterparts as *ext* (if at least one inspector marks the object as *ext*) and 2280 as *ptl* (if both inspectors classify the object as *ptl*). We rejected 238 *mcl* and 183 stars (83 of them are spectroscopically confirmed and the rest confirmed from their SEDs, see Sect. 3). From both visual classifications, it is clearly seen that stars typically have magnitudes less than ∼16 mag, and *mcl* counterparts dominate the sources with magnitudes above ∼25 mag. This kind of visual inspection was necessary to reject bad counterparts and to have an idea of how to choose the photometric templates. The final classification of the sources was made on the basis of spectroscopic information, SEDs, and/or X-ray luminosities (see Sects. 3 and 4.1 for the details).

In the XMM-LSS catalogs (Chiappetti et al. 2005, 2012; Pierre et al. 2007), each selected multiwavelength counterpart of an X-ray source is assigned a probability, $probXY = 1 - \exp(-\pi n(<m) r^2)$, where r is the angular distance between the X-ray source and its counterpart and $n(<m)$ is the density of objects brighter than the magnitude m of the counterpart. The random probability of association between an X-ray source and a counterpart Y is given by *probXY* (Downes et al. 1986), where $Y = O, I, \ldots$ for an optical, infrared, etc. counterpart. The median value of *probXO* for *ext*, *ptl*, stars, and *mcl* objects is 0.018, 0.009, 0.0002 and 0.109, respectively. Tajer et al. (2007) and Garcet et al. (2007) ranked the probability of counterparts as good ($probXY < 0.01$), fair ($0.01 < probXY < 0.03$) and bad ($probXY > 0.03$). We thus see that our *mcl* objects naturally fall in the latter category.

[3] The data are available in the Milan DB in the 2XLSSd and 2XLSSOPTd tables. See Chiappetti et al. (2012) for details.
[4] *Spitzer* Wide-area InfraRed Extragalactic legacy survey: http://swire.ipac.caltech.edu//swire/swire.html
[5] Infrared Array Camera on the *Spitzer* Space Telescope.
[6] The Multiband Imaging Photometer for *Spitzer*.
[7] The UKIRT Infrared Deep Sky Survey: http://www.ukidss.org/
[8] The Galaxy Evolution Explorer: http://www.galex.caltech.edu/

Table 1. Photometric redshift accuracy and fraction of the outliers for the samples of selected objects, which have 4 and more (4+), etc. of photometric bands.

	ext			*ptl*			*all*		
Sample	$N_{\rm tot}$ ($N_{\rm sp}$)	$\sigma_{\Delta z/(1+z_{\rm sp})}$	η,%	$N_{\rm tot}$ ($N_{\rm sp}$)	$\sigma_{\Delta z/(1+z_{\rm sp})}$	η,%	$N_{\rm tot}$ ($N_{\rm sp}$)	$\sigma_{\Delta z/(1+z_{\rm sp})}$	η, %
4+ bands	2234(259)	0.057	11.2	2201 (505)	0.091	27.6	4435 (764)	0.076	22.6
7+ bands	1330 (243)	0.057	10.4	1725 (500)	0.087	26.7	3055 (718)	0.074	21.8
9+ bands	415 (130)	0.057	7.7	570 (226)	0.074	22.1	985 (356)	0.063	16.9
7+ and PDZ = 100	743 (195)	0.052	7.3	1072 (373)	0.074	23.9	1815 (568)	0.065	18.1
7+ and $i' < 22$	819 (209)	0.057	8.1	1278 (334)	0.076	25.0	2097 (635)	0.071	20.0

3. Photo-*z* determination

For the photo-z determination, we used the LePhare[9] public code (Arnouts et al. 1999; Ilbert et al. 2006). First of all, we compiled a training sample of objects with known spectroscopic redshifts. The spectroscopic redshifts for the XMM-LSS field sources were taken from the papers, which are listed in the description of columns for Table 2. We only took into consideration those redshifts for which the angular separation between the optical counterpart of the X-ray source and the object observed spectroscopically is less than 1″. We also visually verified that the coordinates associated with the spectra correspond to those of our optical counterparts. We found 783 spectroscopic redshifts for the optical counterparts, which were classified as galaxies and AGN/QSOs. We did not consider 51 of the redshifts, which have a rank "3", as seen in the description of columns for Table 2. We have to note that an inhomogeneity of the spectroscopic data could affect the final accuracy of the photo-spectro-z relation, but we used all available information at this time.

The photo-z calculation was performed using 11 bands: u^*, g', r', i', z' (CFHTLS); J and K (UKIDSS); 3.6 and 4.5 μm (Swire/IRAC); and far-UV and near-UV bands of GALEX. As recommended by the authors of LePhare, we did not use bands above $\lambda > 5$ μm. Indeed, the templates used for the Spectral Energy Distribution (SED) fitting are not reliable at those wavelength. For all the sources of the sample, we used the total magnitudes for all bands in the AB photometric system and consider the Galactic extinction using $E(B-V)$ values, according to the Schlegel (1998) maps, and the Cardelli (1989) extinction law with $R_v = 3.1$.

As described in Salvato et al. (2011) we separately considered two samples of objects, according to our visual classification. As noted above, we denote extended as *ext* (we assume that this sample mostly consists of galaxy dominated objects), and point-like as *ptl* (AGN/QSO dominated sample). The photometric redshift calculation was performed using the Salvato et al. (2009) templates for our *ptl* and *ext* objects with $F_{(0.5-2\ \rm keV)} > 8 \times 10^{-15}$ erg s^{-1} cm^{-2} and using the Ilbert et al. (2009) templates for the rest of the fainter X-ray objects by following the flow-chart (Fig. 8) by Salvato et al. (2011). The only differences between the calculations are that we did not apply any variability correction and did not use the prior $-30 < M_{\rm abs} < -22$ for *ptl*. Extinction laws, according to Calzetti et al. (2000) and Prevot et al. (1984), were applied to the Ilbert et al. (2009) normal galaxy templates as free-fitting parameters. To the Salvato et al. (2009) templates, we applied only the Prevot et al. (1984) extinction law. We computed the intrinsic galactic absorption $E(B-V)$ from 0.00 to 0.40 by steps of 0.05. For the redshift calculation, we used a range from 0 to 6 with a step $\Delta z = 0.01$ and a step $\Delta z = 0.05$ at redshifts 6–7. We added the emission lines to normal galaxy templates as in Ilbert et al. (2009).

We defined stars following the condition by Salvato et al. (2011): $1.5 \times \chi^2({\rm STAR}) < \chi^2({\rm AGN/GAL})$, where $\chi^2({\rm STAR})$ and $\chi^2({\rm AGN/GAL})$ are the reduced χ^2 for the best-fit solutions obtained with stellar and AGN or galaxy libraries, respectively. We found 183 stars, in which 83 of these were spectroscopically confirmed.

We estimated the photometric redshift accuracy using the measurement $\sigma_{\Delta z/(1+z_{\rm sp})}$, which according to Hoaglin et al. (1983) is given by

$$\sigma_{\Delta z/(1+z_{\rm sp})} = 1.48 \times \frac{\rm median|z_{ph} - z_{sp}|}{(1 + z_{\rm sp})}. \quad (1)$$

The outliers are defined as those objects for which $|(z_{\rm ph}-z_{\rm sp})/(1+z_{\rm sp})| > 0.15$.

In Table 1, we show the values of the accuracy $\sigma_{\Delta z/(1+z_{\rm sp})}$ and of the fraction of the outliers η for the different samples of *ext* and *ptl*, *all*=*ext*+*ptl* objects, and the numbers of objects in each sample. As expected, the accuracy of photo-z for the *ext* objects is much better than for *ptl*. As the sources are extended, they must be at a lower redshift, and the galaxy component must be non negligible. It is well known that the accuracy of photo-z for normal galaxies is very high below redshift 1.5. It also has few optical bands that are able to grasp the typical features of the SED (i.e., the 4000 Å break). On the contrary, point-like sources are at a higher redshift, and the galaxy component is fainter than the power-law SED that describes the bright nucleus. For these sources, intermediate band photometry would be necessary for identifying the emission lines and would break the degeneracy among the possible redshift solutions (see Salvato et al. 2009, Table 4). For example, we have $\sigma_{\Delta z/(1+z_{\rm sp})} = 0.057$, 0.091, and 0.076 with $\eta = 11.2\%$, 27.6%, and 22.6%, respectively, for the *ext*, *ptl*, and *all* samples of objects with 4 or more bands (4+). We did not apply any magnitude cut to our samples. Only 6% of our objects are fainter than $i' = 24.5$ and 0.4% are fainter than $i' = 26.0$ mag. We see that the accuracy of the photometric redshifts is increasing with the increasing number of bands.

In addition to the computation of the best photometric redshift solution, LePhare provides the redshift probability distribution (PDZ). For a high available number of bands, the redshift solution appears as a clear peak with a PDZ near or equal to 100. When decreasing the number of bands and increasing error in photometry, the PDZ presents either multi-peaks or a unique large distribution of possible solutions. We used the information in the PDZ for rejecting unreliable solutions, when two or more solutions for one object were produced. From Table 1, we see the following: if we consider objects with 7 and more (7+) bands with PDZ = 100, then $\sigma_{\Delta z/(1+z_{\rm sp})}$ and η are practically the same as for the sample of objects having 9 or more (9+) bands. In the case of 9+ bands the number of objects are, however, less than twice that of the case of 7+ bands with PDZ = 100. In the

[9] http://www.cfht.hawaii.edu/~arnouts/LEPHARE/lephare.html

Table 2. List of an extracted sample of X-ray sources with optical counterparts and their redshifts.

2XLSSd	Ora	Odec	z_{sp}	zsprank	zspref	zspclass	z_{ph}	sedclass	zphrank	*HR*	L_{Xsoft}	L_{Xhard}	final_class	dogflag
(1)	(2)	(3)	(4)	(5)	(6)	(7)	(8)	(9)	(10)	(11)	(12)	(13)	(14)	(15)
J022006.8-045422	35.0288	–4.9060	null	null	null	null	0.92	gal	1	–1	3.0×10^{42}	null	AGN/QSO	0
J022008.7-045906	35.0364	–4.9849	1.65	1	4	AGN	1.55	agn/qso	1	–0.64	1.3×10^{44}	1.9×10^{44}	AGN/QSO	0
J022327.8-040119	35.8661	–4.0220	1.92	1	2	AGN	1.88	agn/qso	1	–0.62	2.9×10^{44}	3.4×10^{44}	AGN/QSO	0
J022500.4-040248	36.2523	–4.0466	0.61	2	5	GAL	1.95	agn/qso	3	–1	4.5×10^{42}	null	AGN/QSO	0
J022624.3-041343	36.6016	–4.2285	null	null	null	null	1.57	agn/qso	2	–1	1.3×10^{44}	null	AGN/QSO	1
J022630.7-040600	36.6274	–4.0998	0.00	1	4	STAR	0.00	star	3	–1	null	null	STAR	0
J022740.6-041857	36.9191	–4.3162	0.73	null	6	GAL	1.74	gal	2	–0.47	1.5×10^{43}	2.6×10^{43}	AGN/QSO	0
J022758.5-040851	36.9936	–4.1475	1.97	2	1	AGN	1.94	agn/qso	3	–1	8.2×10^{43}	null	AGN/QSO	0

Notes. This is an example for several sources from the main catalog. (1) 2XLSSd name; (2) RA of the optical counterpart; (3) Dec of the optical counterpart; (4) spectroscopic redshift when available; (5) rank of the spectroscopic redshift: 1 – good quality (two or more lines in the spectra); 2 – acceptable redshifts (one clear line in the spectra); 3 – dubious redshift; (6) source of the spectroscopic redshift: 1 – Le Fèvre et al. (2005); 2 – Garcet et al. (2007); 3 – Lacy et al. (2007); 4 – Stalin et al. (2010); 5 – Lidman et al. (2012); 6 – the NASA/IPAC Extragalactic Database: http://nedwww.ipac.caltech.edu (NED); 7 – Simpson et al. (2006, 2012); 8 – Geach et al. (2007); 9 – Ouchi et al. (2008); 10 – Smail et al. (2008); 11 – van Breukelen et al. (2007, 2009); 12 – Finoguenov et al. (2010); 13 – Akiyama et al. (in prep.); 14 – Croom et al. (in prep.). The compilation of redshifts from 7–14 can be found here: http://www.nottingham.ac.uk/~ppzoa/UDS_redshifts_18Oct2010.fits; 15 – SDSS DR9 data: http://www.sdss3.org. We did not use the SDSS redshifts in the calculations; they were added to the table later. (7) spectral classification; (8) photometric redshift; (9) classification according to SED: GAL – normal galaxy templates of Ilbert et al. (2009) or templates #1–6 of Salvato et. al (2009), AGN/QSO – hybrid and AGN/QSO templates (#7–30) of Salvato et al. (2009); (10) rank of the photometric redshift: 1 – good quality photometric redshift: 7 or more bands, *PDZ* = 100; 2 – medium quality photometric redshift: 7 or more bands, PDZ< 100; 3 – dubious photometric redshift, 4–6 bands; 4 – no redshift because of lack of photometry; 5 – no redshift because the objects are invisible (very faint) or wrong associations (probably misclassified); (11) hardness ratio *HR*; (12) X-ray luminosity in the soft band, erg/s; (13) X-ray luminosity in the hard band, erg/s; (14) final classification of the source; (15) DOGs objects are flagged by 1 (see Sect. 4.3 for the details).

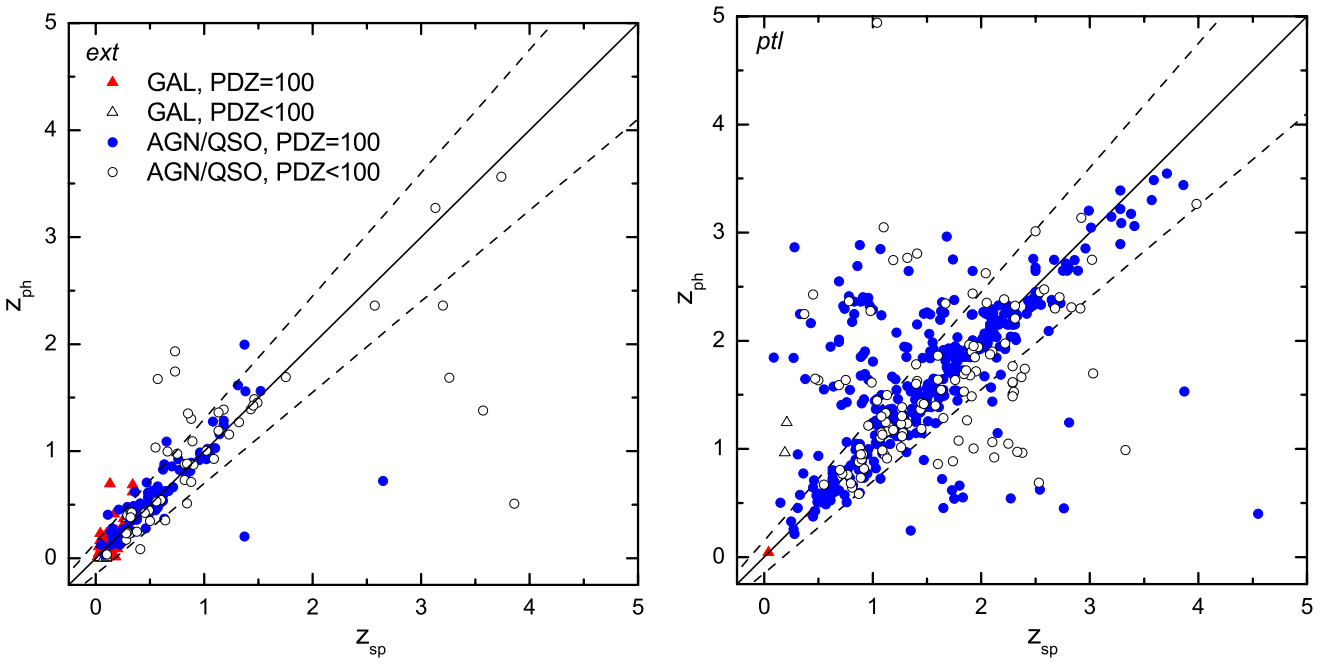

Fig. 3. Photo-z (7+ bands) vs. spectro-z for the 243 visually classified extended objects (*left panel*) and the 479 *ptl* objects (*right panel*). The solid lines correspond to $z_{ph} = z_{sp}$, and the dashed lines correspond to $z_{ph} = z_{sp} \pm 0.15 \times (1 + z_{sp})$. PDZ represents the parameter appearing in the probability distribution of z given by LePhare. When PDF = 100, the solution is unique.

last row of Table 1, we show the accuracy of photo-z for the magnitude-limited sample with $i' < 22$. We see that the accuracy of photo-z is only negligibly better than for the whole 7+ bands sample.

The relations between spectroscopic and photometric redshifts for the *ext* and *ptl* objects that have 7+ bands are presented in the left and right panels of Fig. 3, respectively. These samples have $\sigma_{\Delta z/(1+z_{sp})}$ values of 0.057 and 0.087 with a fraction of outliers of 10.4% and 26.7%, respectively. The number of objects with PDZ < 100 do not exceed 41% of the total number of objects. Meanwhile, the number of outliers among these objects are only 34%.

We list hereafter some statistics: 85% of our *ext* objects were fitted with normal galaxy templates (the rest with AGN/QSO hybrid templates) and 74% of *ptl* were fitted with templates having an AGN/QSO contribution (the rest with normal galaxy

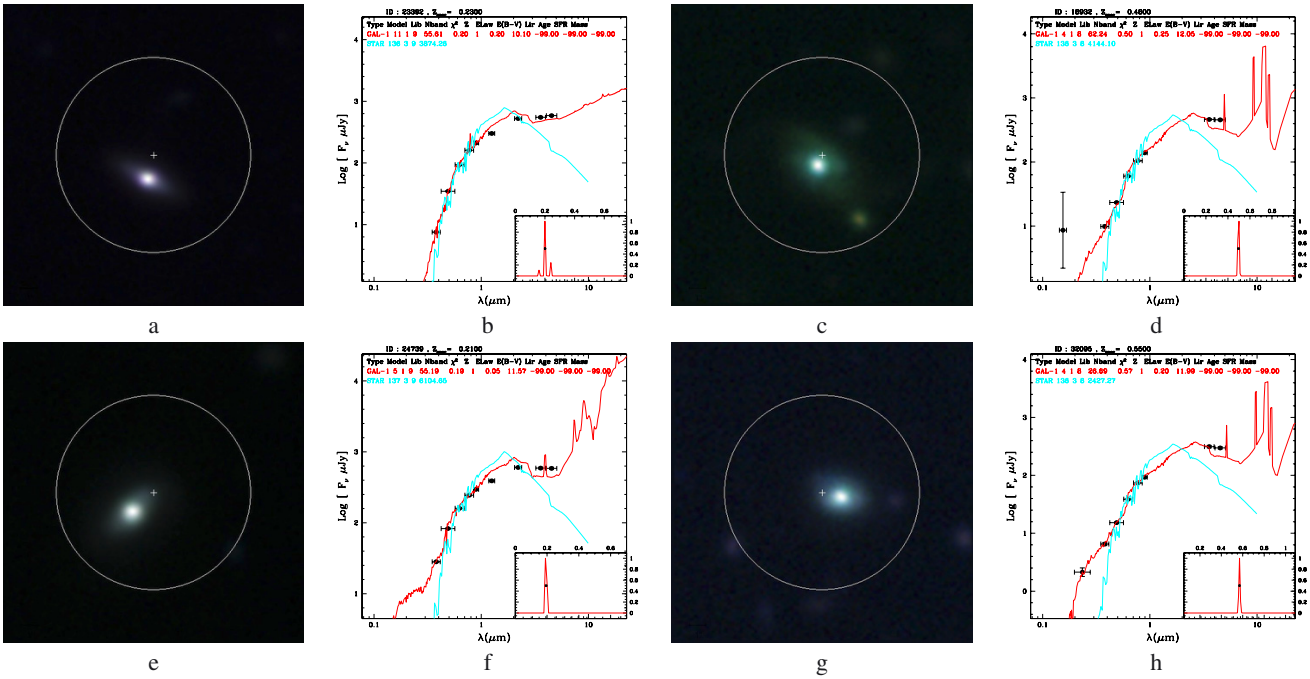

Fig. 4. Examples of optical CFHTLS images and SEDs for selected objects from the *ext* sample fitted with hybrid AGN contaminated templates. The color images are composed of the g', i' and r' band images. Below we list the spectro-z, the source of the spectral classification, and the estimated photo-z for each pair of images: $z_{sp} = 0.23$ by Stalin et al. (2010), $z_{ph} = 0.15$ **a)**, **b)**; $z_{sp} = 0.478$ by Simpson et al. (2012), $z_{ph} = 0.496$ **c)**, **d)**; $z_{sp} = 0.205$ by Garcet et al. (2007), $z_{ph} = 0.195$ **e)**, **f)**; $z_{sp} = 0.550$ by Simpson et al. (2012), $z_{ph} = 0.569$ **g)**, **h)**. The radius of the white circle is 6″.

templates). In Fig. 4, we show Seyfert galaxies with clearly visible hosts and bright AGN. These objects are typical examples of X-ray sources that look like extended at optical wavelengths and have optical spectra and SEDs with an AGN/QSO contribution. Table 2 presents a small fragment of data that is available through the Milan DB[10] and the Centre de Données de Strasbourg (CDS[11]) for all 5142 considered objects.

In this paper, we considered the properties of only 3071 objects that have spectroscopic or photometric redshifts with rank 1 or 2 (see definitions in the description of columns for Table 2). Their redshift distribution is shown in the bottom panel of Fig. 5. The top panel of Fig. 5 presents the redshift distribution of 196 GALs and 2875 AGN/QSOs (the final classification is described in the next subsection). The median redshifts for the whole sample, GALs, and AGN/QSOs are 1.20, 0.19, and 1.27, respectively. We excluded 52 extended X-ray objects, so they are not represented in Fig. 5.

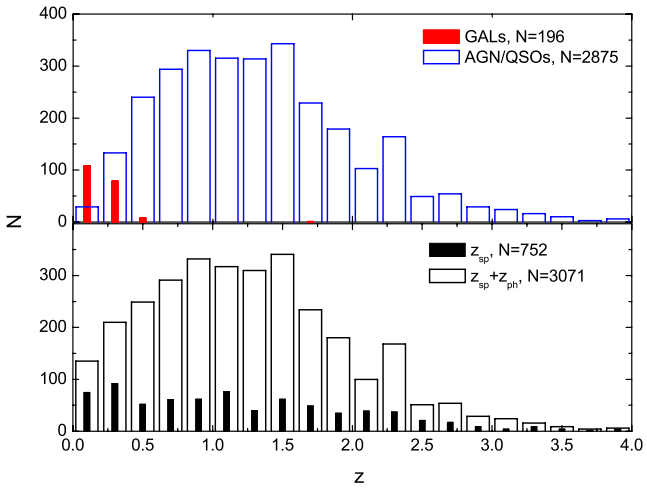

Fig. 5. *Lower panel*: redshift distributions of all objects with known spectro-z or photo-z (white histogram) and of objects with spectro-z (black histogram). *Upper panel*: redshift histogram of sources classified as GALs or AGN/QSOs from the $z_{sp} + z_{ph}$ sample.

4. X-ray and multiwavelength properties of selected objects

4.1. X-ray luminosity

Figure 6 shows the X-ray luminosity of the sources, L_X, as a function of their redshift. The K-correction was applied to L_X, according to Burlon et al. (2011). We mark "GAL" for all spectroscopically confirmed or photometrically classified galaxies (SEDs fitted by normal galaxy templates by Ilbert et al. 2009 or templates #1–6 by Salvato et al. 2009). The exception is for sources with $L_{X,hard} > 2\times10^{42}$ erg/s (or $L_{X,soft} > 10^{42}$ erg/s if the X-ray source was observed only in the soft band) that we consider AGN/QSOs, as noted in Brusa et al. (2010). We also refer to an object as AGN/QSO if it has a spectrum or a SED typical of an AGN or QSO. We have 196 (6.4%) GALs and 2875 (93.6%) AGN/QSOs that are in good correspondence with the COSMOS survey (6.3% of X-ray galaxies, Brusa et al. 2010). X-ray luminosities and final classification of all considered sources are noted in the last column of Table 2. We note that the final sample of GALs consists of 97% of visually classified *ext* objects and 3% of *ptl* objects while the final sample of AGN/QSOs consists of 39% and 61% of *ext* and *ptl*, respectively.

Among the hard X-ray objects (those which have a flux in the 2−10 keV band) we selected a subsample of sources with

[10] http://cosmosdb.iasf-milano.inaf.it/XMM-LSS/
[11] http://cdsweb.u-strasbg.fr

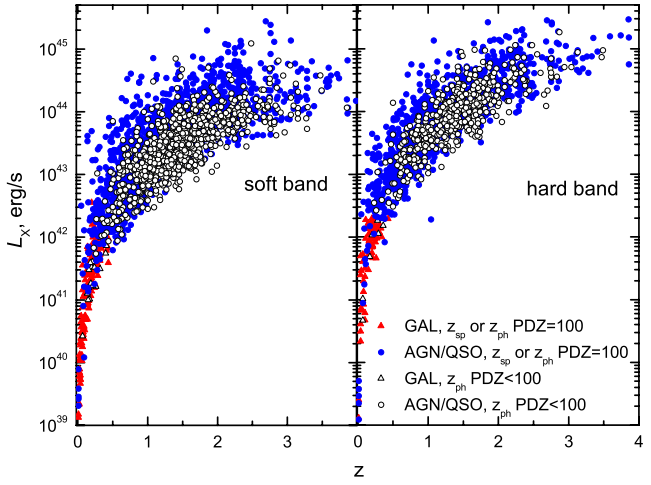

Fig. 6. X-ray luminosity vs. redshift (photo and spectro) for the soft and hard bands.

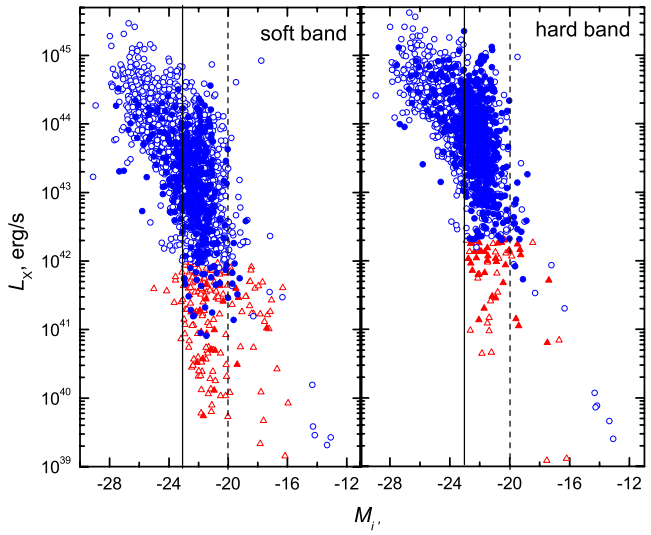

Fig. 7. Dependence on X-ray luminosity vs. absolute magnitude in the i'-band. GALs are marked with triangles and AGN with circles. Soft ($HR < -0.2$) sources are shown with open symbols and hard ($HR \geq -0.2$) sources with filled symbols. The solid vertical lines $M_{i'} = -23.5$ divide the AGN from the brighter QSOs. In the overdensity analysis (Sect. 5), we have only considered the sources locating between the solid and dashed vertical lines.

X-ray to optical ratio[12] X/O > 10. This characteristic indicator is important to identify highly obscured AGN/QSOs (see for example Fiore et al. 2003; Mignoli et al. 2004; Brusa et al. 2005, 2010). Our sample consists of 252 highly obscured AGN/QSO candidates which represents 11% of the total AGN/QSO and 8% of the whole sample. In Fig. 7, we present the X-ray luminosity vs. $M_{i'}$ absolute luminosity for GALs and AGN/QSOs, where the vertical solid lines $M_{i'} = -23.5$ divide the AGN from the brighter QSOs. This limit is very close to the classical definition ($M_B = -23$). It is seen that the hard ($HR \geq -0.2$) sources (filled symbols) are less bright than the soft ($HR < -0.2$) ones.

[12] As in Brusa et al. (2005) the X/O ratio was calculated as in with the r-band transformed into a R-band using the empirical Lupton et al. (2005) relation.

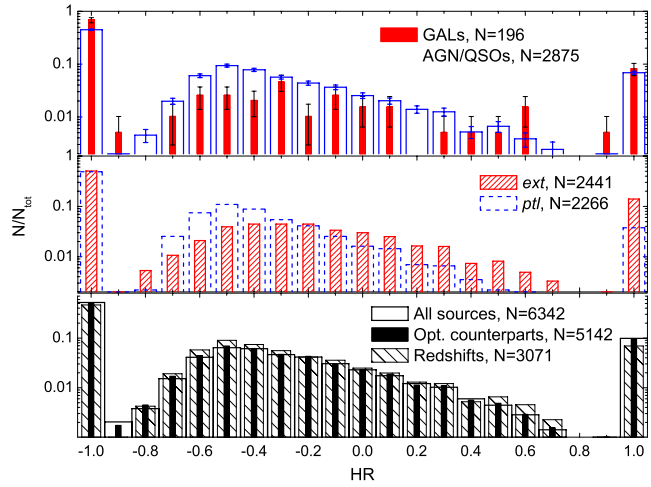

Fig. 8. Distributions of the fractional number of XMM-LSS X-ray sources as a function of their hardness ratio: (i) for the cases of all X-ray sources, X-ray sources with optical counterparts, X-ray sources with spectro-z or photo-z (*bottom panel*); (ii) *ext* and *ptl* objects according to our visual classification (*middle panel*); (iii) GALs and AGN/QSOs according to spectroscopy, SEDs and/or L_X criteria (*top panel*).We plot Poisson uncertainties only in the *upper panel* for clarity.

4.2. The hardness ratio

The bottom panel of Fig. 8 presents the comparison of the XMM-LSS source distributions vs. their hardness ratio $HR = (H - S)/(H + S)$, where S and H denote the count rate (cts/s) in the soft and the hard bands, respectively. Considering the average errors of the count rates measurements, we estimate a typical uncertainty for HR of 0.1. We considered distributions of all the sources from the X-ray catalog, sources with optical counterparts, and sources with spectro- or photo-z. We see that the various distributions look similar, so we do not see any distinction in the distributions between X-ray sources showing an optical counterpart or not. That is the Kolmogorov-Smirnov probability that distributions are the same is 0.92. The middle panel of Fig. 8 presents the distribution of HR for the sources, which were visually classified as extended *ext* and point-like *ptl*. We may compare it with the upper panel, where the distributions of HR for GALs and AGN/QSOs are shown. We see that *ext* sources show some excess of sources with $HR \geq -0.2$ in comparison with the *ptl* sample.

The upper panel of Fig. 8 shows the distributions of HR for GALs and AGN/QSOs. The samples of GAL and AGN/QSOs contain 62% and 45%, respectively, of the sources observed only in the soft band. The total source sample contains ~46% of objects, a fraction that is significantly higher than that of the COSMOS survey (~17%; Brusa et al. 2010) without a hard band detection. We see that some objects, which appear as extended at optical wavelengths, have a hard spectrum and could be considered as candidates for obscured AGN. We plan to consider the properties of their host galaxies in a separate work.

The Kolmogorov-Smirnov probabilities that the HR distributions are drawn from the same parent population for the pairs of samples: *ext* – *ptl* and GAL – AGN/QSO are less than 10^{-10} and 10^{-5}, respectively. The median HR values in the corresponding quartile ranges for all sources, AGN/QSOs, and GALs are $-0.63^{+0.34}_{-0.37}$, $-0.60^{+0.32}_{-0.40}$ and $-1^{+0.55}_{-0.00}$, respectively. Note that 133 GALs out of the total of 196 in total were not observed in the hard band.

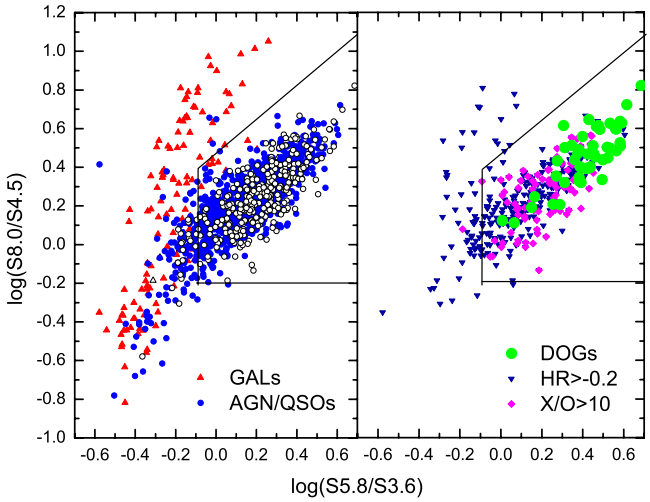

Fig. 9. IRAC color–color plot. GALs and AGN/QSOs on the *left panel* (open symbols correspond to objects which have photo-z with PDZ < 100, as in Fig. 6). DOGs, $HR \geq -0.2$ and X/O > 10 sources are shown on the *right panel*.

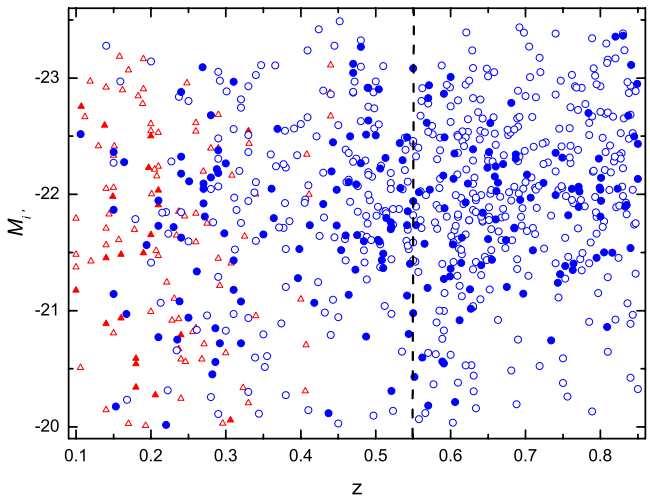

Fig. 10. Diagram showing the absolute i'-band magnitude versus redshift for our final volume limited all sample. GALs are marked with triangles; AGN with circles. Soft ($HR < -0.2$) sources are shown with open symbols, and hard ($HR \geq -0.2$) sources with filled symbols. The dashed line marks the separation between two chosen redshift ranges.

It is known that there are 80% of spectroscopically confirmed obscured QSOs among sources with $HR \geq -0.2$ (see for example Ghandi et al. 2004, Brusa et al. 2010 and references therein). We have 641 (21%) of the objects with $HR \geq -0.2$ (606 of them are AGN/QSOs) while 154 of them (24%) also have X/O > 10; these objects are faint at optical wavelengths and very bright in hard X-rays.

4.3. Infrared colors

Lacy et al. (2004) proposed a useful approach for the classification of AGN with the help of a *Spitzer*/IRAC color–color diagram: AGN/QSOs were concentrated within a compact region of this a diagram (see also Stern et al. 2005; Lacy et al. 2007; Brusa et al. 2009, 2010). In total 1467 (51%) AGN/QSOs and 117 GALs (60%) were observed in all 4 IRAC bands. The left panel of Fig. 9 presents the color–color plots for AGN/QSOs and GALs. We find that 1322 (91%) of the AGN/QSOs and 19 (16%) of the GALs are lying in the AGN region.

Dey et al. (2008) and Brodwin et al. (2008) have proposed to select a population of high-redshift dust-obscured galaxies (DOGs) with large mid-infrared to ultraviolet luminosity ratios using simple criteria: $F_{24\,\mu m} \geq 0.3$ mJy and $(R - [24]) \geq 14$ (Vega) mag, where $[24] \equiv -2.5 \log_{10}(F_{24\,\mu m}/7.29\,\mathrm{Jy})$. Using these criteria, these authors found 2603 DOG candidates in the NOAO Deep Wide-Field Survey Bootes area with 86 objects of their sample having $\langle z \rangle = 1.99$ with $\sigma = 0.45$. We have applied the Dey et al. (2008) criteria and found 54 DOG candidates, which consist of 1.7% of our sample. Their average redshift is lower than that of Dey's objects: $\langle z \rangle = 1.67$ with $\sigma = 0.39$. However, this value is higher than that of the total sample, where $\langle z \rangle = 1.27$ with $\sigma = 0.75$ (see the z distribution in Fig. 5). In the right panel of Fig. 9, we show the DOGs, hard objects with $HR \geq -0.2$ and objects with X/O > 10. We see that the DOGs are concentrated in the upper corner of the AGN region, while $HR \geq -0.2$ and obscured QSOs with X/O > 10 are located in and near the AGN region. Finally, we note that 13 are DOGs out of the 154 $HR \geq -0.2$ and X/O > 10 objects. All DOGs are marked with an "1" in the last column of Table 2.

5. Environmental properties of the X-ray point-like sources

We investigate the galaxy environment of our X-ray selected point-like sources. To this end, we use the CFHTLS W1 optical object catalog[13], but we only consider galaxies with a star/galaxy classification index CLASS_STAR < 0.95 and with the i'-band limiting magnitude of 23.5, which is near the catalog completeness limit[14]. We have ignored the sources from the ABC fields (see Fig. 1), because these areas were not observed in the i'-band. Thus, the considered area in the environmental studies only concerns ~9 sq. deg.

Considering the completeness limits of the CFHTLS and of our X-ray sample, we investigate the environment of X-ray sources in a volume limited region of their optical counterparts. This is defined by the redshift range of $0.1 \leq z \leq 0.85$ for which their optical counterparts are within the absolute magnitude range $-23.5 < M_{i'} \leq -20$ (while the apparent rest-frame magnitude of the knee of the i'-band luminosity function has $m^* < 22.5$; see Eq. (2)). The luminosity limits can be seen in Fig. 7 in the L_X vs. $M_{i'}$ plots. We consider the following different subsamples of X-ray sources: all, GALs (only in the $0.1 \leq z \leq 0.55$ redshift range), AGN, soft ($HR < -0.2$) AGN and hard ($HR \geq -0.2$) AGN. We expect that the overwhelming majority of our soft AGN are unobscured and that hard AGN are obscured. In Fig. 10, we present the $M_{i'}$ vs. z distribution of all selected objects ($N = 777$). We note that the accuracy of the photometric redshifts for this sample is $\sigma_{\Delta z/(1+z_{sp})} = 0.061$ with $\eta = 13.8\%$. We did not reject the objects with PDZ < 100, because the number of these objects in our low redshift sample do not exceed 17% (only 34% of objects with PDZ < 100 are outliers). In any case, we repeated all calculations, excluding the dubious photo-z, and we reached the same conclusions.

[13] http://www3.cadc-ccda.hia-iha.nrc-cnrc.gc.ca/community/CFHTLS-SG/docs/cfhtlswide.html#W1
[14] http://terapix.iap.fr/cplt/T0006-doc.pdf

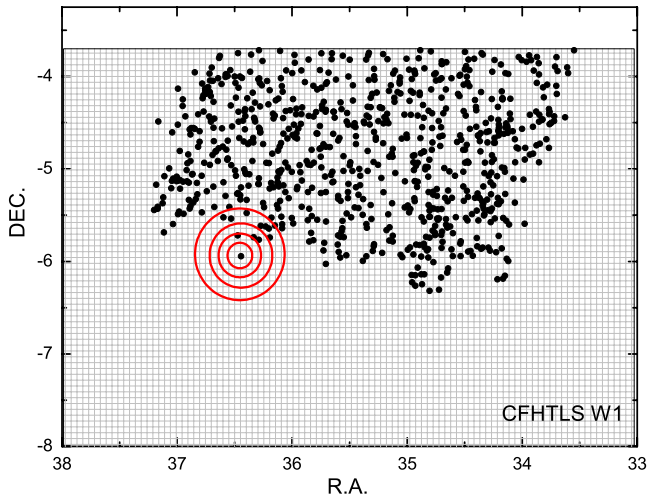

Fig. 11. The CFHTLS W1 field and corresponding 777 XMM-LSS sources. An example of the annuli for one source is shown.

5.1. Overdensity measures

To calculate the optical galaxy overdensity around an X-ray source, we consider concentric annuli centered on each source (see an example in Fig. 11). By considering their redshift and angular distance D_A, we estimate the linear sizes of the annuli at the source's rest-frame distance. Then we count the number, N_i, of CFHTLS galaxies within a given annulus in the range of magnitudes from m^* to $m^* + \Delta m$ (hereafter fainter galaxies) or from $m^* - \Delta m$ to m^* (hereafter brighter galaxies), where m^* is the apparent magnitude corresponding to the knee of the i'-band luminosity function [$\Phi(L)$] given by

$$m^* = 5\log_{10} d_L + 25 + M^*_{i'} + Q_{0.1}(z) + K_{0.1}(z), \quad (2)$$

with $M^*_{i'}(=-20.82 + 5\log_{10} h)$ is the absolute magnitude of the knee of the i-band $\Phi(L)$ taken from Blanton et al. (2003b). $Q(z)$ and $K(z)$ are the evolution and K-corrections, respectively, taken from Poggianti et al. (1997) and shifted to match their rest-frame shape at $z = 0.1$; d_L is the luminosity distance.

Next, we have calculated the galaxy overdensities, δ_i, within each annulus as

$$\delta_i = \frac{N_i}{f_i N_b} - 1, \quad (3)$$

where N_i is the total number of objects within the ith radial annulus with surface area A_i. N_b is the local background counts, estimated in the spherical annulus between 3.1 and 5 Mpc, with surface area A_b, and f_i is the normalization factor that normalizes the background counts to the area of each spherical annulus. It is given by

$$f_i = \frac{A_i}{A_b}. \quad (4)$$

Therefore we obtain the overdensity profile, $\delta_i(r)$, as a function of the source-centric distance r, for each X-ray source. The Poissonian uncertainty of the overdensity, δ_i, is given by

$$\sigma^2_{\delta_i} = \frac{1+\delta_i}{N_b}\left(\frac{1}{f_i} + 1 + \delta_i\right). \quad (5)$$

To estimate the significance of the results, we compare the overdensity of galaxies around each of our sources with the expected in mock X-ray source distributions, which have random coordinates but the same fiducial magnitude (m^*), which is estimated from the redshift of the X-ray source itself. For the mock, randomly distributed sources, we used the same CFHTLS optical catalog as we did for the real ones.

As an example, we find that the mean overdensity of the all sample within $0.1 \le z \le 0.55$ and for the first radial annulus is 0.23 ± 0.80 [15], while the corresponding value is 0.04 ± 0.75 for the random distribution. Clearly, the apparent wide scatter hinders our ability to distinguish environmental sample differences based on the mean overdensity.

As a more sensitive alternative, we use a Kolmogorov-Smirnov (KS) two-sample test to quantitatively estimate the differences between the real and random overdensity distributions constructed for each radial distance annulus. In effect we use the cumulative overdensity distribution,

$$F(>\delta) = N(>\delta)/N_{tot},$$

which is defined as the fraction of all sources (N_{tot}) having an overdensity above a given δ. For the creation of the random overdensity distribution, we have generated 100 random catalogs using the procedure described above. For each catalog, we calculated the cumulative overdensity distribution $F(>\delta)$. Then we averaged these 100 distributions and obtained the final random distribution for which we compared with the real one.

Figure 12 shows the cumulative overdensity distributions for the real and mock samples, for the 0–0.4 Mpc and the 0.4–0.8 Mpc radial annuli, for the fainter ($m^* < m < m^* + 1$) and brighter ($m^* - 1 < m < m^*$) galaxy environments and in the two $0.1 \le z \le 0.55$ and $0.55 < z \le 0.85$ redshift ranges (see labels in each figure). Table 3 presents the corresponding KS probabilities ($\mathcal{P}$) of the real and mock samples being drawn from the same parent population.

Although our results show that X-ray point-like sources inhabit both dense and underdense environments, there are significantly more sources inhabiting overdense regions. In all samples, we find that $F(\delta > 0) \gtrsim 55\%$ for the first radial annuli (0–0.4 Mpc) with the random expectation being always <45% (Table 4). For the case of the all sample, for example, in the $0.1 \le z \le 0.55$ redshift range and for the 0–0.4 Mpc radial annulus, we find that the fraction of sources with positive overdensity, $F(\delta > 0)$, is 58 ± 4%/66 ± 4% for the fainter/brighter

Table 3. Kolmogorov-Smirnov probabilities ($\mathcal{P}$) of the real and mock sample overdensity distributions (in the two indicated radial annuli) being drawn from the same parent population for the fainter ($m^* < m < m^* + 1$) and brighter ($m^* - 1 < m < m^*$) galaxy environments and in the two redshift ranges.

Sample	N	$m^* < m < m^* + 1$		$m^* - 1 < m < m^*$	
		$\mathcal{P}_{0-0.4\ \mathrm{Mpc}}$	$\mathcal{P}_{0.4-0.8\ \mathrm{Mpc}}$	$\mathcal{P}_{0-0.4\ \mathrm{Mpc}}$	$\mathcal{P}_{0.4-0.8\ \mathrm{Mpc}}$
		$0.1 \le z \le 0.55$			
All	375	3.7×10^{-6}	1.3×10^{-5}	1.9×10^{-20}	1.7×10^{-8}
GAL	105	3.4×10^{-2}	3.5×10^{-1}	1.8×10^{-10}	6.1×10^{-1}
AGN	270	4.7×10^{-5}	2.1×10^{-3}	8.7×10^{-11}	1.6×10^{-4}
Soft AGN	170	1.6×10^{-3}	9.3×10^{-1}	5.3×10^{-7}	6.2×10^{-2}
Hard AGN	100	5.0×10^{-3}	1.0×10^{-1}	1.9×10^{-4}	6.2×10^{-1}
		$0.55< z \le 0.85$			
All	402	7.6×10^{-5}	6.7×10^{-5}	1.7×10^{-3}	3.0×10^{-4}
Soft AGN	307	1.4×10^{-4}	4.2×10^{-3}	6.8×10^{-3}	3.8×10^{-4}
Hard AGN	95	2.6×10^{-1}	7.8×10^{-1}	4.5×10^{-2}	5.8×10^{-1}

[15] The error here is the variance of overdensities over the given sample.

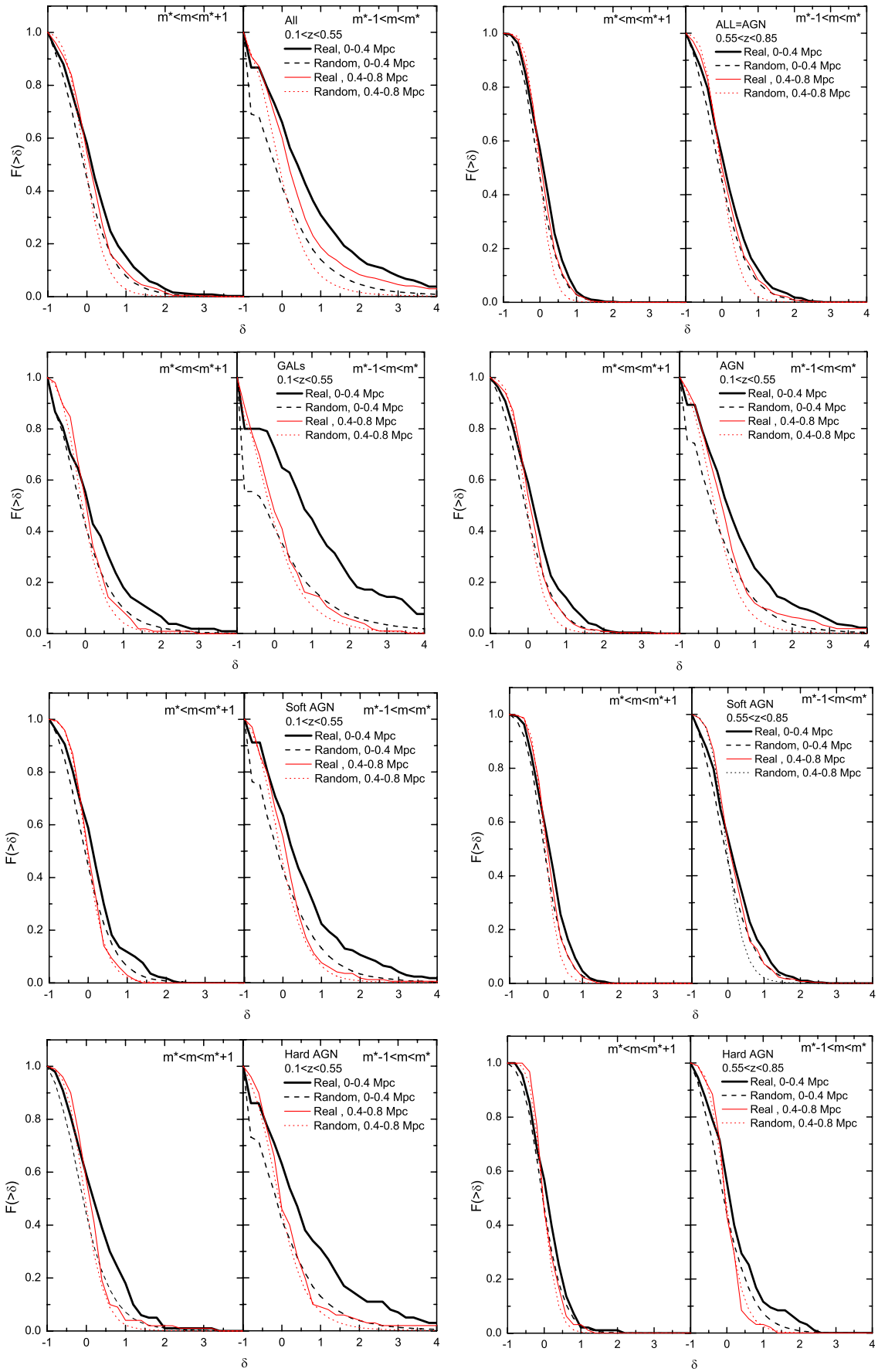

Fig. 12. Cumulative distributions of overdensities for the real and mock samples, for the 0−0.4 Mpc and the 0.4−0.8 Mpc radial annuli, for the fainter $m* < m < m* + 1$ and brighter $m* - 1 < m < m*$ environments in the two $0.1 \leq z \leq 0.55$ (*left column*) and $0.55 < z \leq 0.85$ (*right column*) redshift ranges (see labels in each figure).

Table 4. Fraction of sources having positive overdensity ($\delta > 0$) for both the real and mock samples (in the two indicated radial annuli), for the fainter ($m^* < m < m^* + 1$) and brighter ($m^* - 1 < m < m^*$) galaxy environments, and for the two studied redshift ranges.

	$F(\delta > 0) \pm \sigma^*$, %			
	$m^* < m < m^* + 1$		$m^* - 1 < m < m^*$	
Sample	0–0.4 Mpc	0.4–0.8 Mpc	0–0.4 Mpc	0.4–0.8 Mpc
	$0.1 \leq z \leq 0.55$			
All	58 ± 4	54 ± 4	66 ± 4	54 ± 4
All_{rand}	45 ± 3	46 ± 4	41 ± 3	44 ± 3
GAL	55 ± 7	52 ± 7	72 ± 8	52 ± 7
GAL_{rand}	42 ± 6	43 ± 6	41 ± 6	43 ± 6
AGN	59 ± 5	54 ± 4	63 ± 5	54 ± 4
AGN_{rand}	45 ± 4	47 ± 4	42 ± 4	45 ± 4
Soft AGN	59 ± 6	49 ± 5	64 ± 6	49 ± 5
Soft AGN_{rand}	44 ± 5	47 ± 5	43 ± 5	45 ± 5
Hard AGN	59 ± 8	57 ± 8	63 ± 8	57 ± 8
Hard AGN_{rand}	44 ± 7	47 ± 7	42 ± 6	45 ± 7
	$0.55 < z \leq 0.85$			
All	57 ± 4	53 ± 4	54 ± 4	50 ± 4
All_{rand}	46 ± 3	47 ± 3	45 ± 3	47 ± 3
Soft AGN	57 ± 4	54 ± 4	54 ± 4	52 ± 4
Soft AGN_{rand}	46 ± 4	48 ± 4	45 ± 4	47 ± 4
Hard AGN	57 ± 8	45 ± 7	56 ± 8	43 ± 7
Hard AGN_{rand}	47 ± 7	46 ± 7	44 ± 7	46 ± 7

Notes. *Here the uncertainty represents Poissonian noise.

environments, while the corresponding random expectation is 45%/41%, respectively (see Table 4 and left top panel in Fig. 12).

Furthermore, the KS test shows significant differences between the all source overdensity distribution and their random expectations for both fainter and brighter environments and for the two first radial annuli (see Table 3). In the third radial annulus (0.8–1.2 Mpc), the probability of an overdensity distribution difference compared to the random case drops to levels ranging from ~0.05 to 0.3 for both types of environments and redshift ranges. We conclude that we cannot identify significant environmental differences from the random expectations at these large scales. Subtle differences could possibly be revealed only with the use of full redshift information of the surrounding galaxies.

An important result of our analysis is that the overdensities in the $0.1 \leq z \leq 0.55$ redshift range are wider and more significant than those in the $0.55 < z \leq 0.85$ range for all our samples. For example, the fraction of all X-ray sources having positive overdensities of brighter galaxies in the 0–0.4 Mpc annulus increases from 54 ± 4% to 66 ± 4% between the higher and lower z-ranges. This effect is clearly seen by inspecting Table 3 and Fig. 13 (upper panel), where we present the ratio of the galaxy overdensity distributions between the lower and higher redshift ranges studied for the all sample. In the lower panel of Fig. 13, we present the corresponding ratio separately for the soft and hard AGN sources, which also show a positive evolution of their galaxy overdensities. A more relevant discussion will be presented further below.

Therefore, there is a positive redshift evolution of the galaxy overdensity amplitude and/or significance within which X-ray sources are embedded. A similar (weak) tendency was reported by Strand et al. (2008) for the environments of the optically selected type I quasars.

Again inspecting Table 4 and Fig. 12, we have another generic result valid for all the considered samples: the overdensities defined by the brighter galaxies are typically larger and

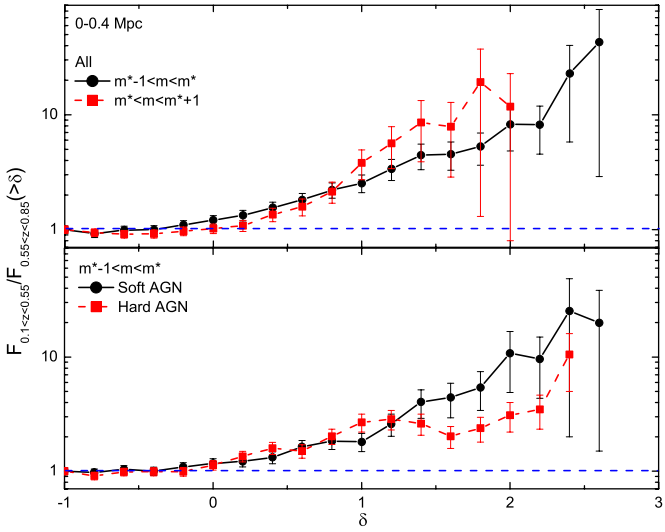

Fig. 13. Ratio of the galaxy overdensity distributions between the lower and higher redshift ranges studied (only in the 0–0.4 Mpc radial annulus). Errorbars correspond to Poissonian uncertainties. *Upper panel*: all sample. *Lower panel*: hard and soft AGN samples (only the brighter environment).

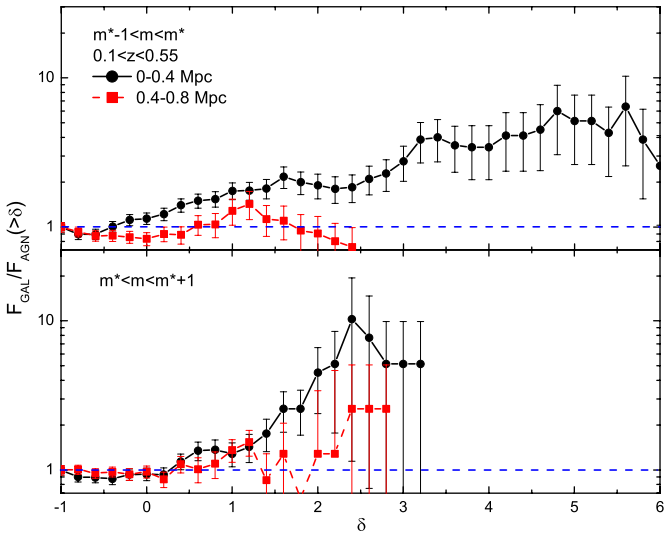

Fig. 14. Ratio of the overdensity distributions of the GAL and AGN samples for both fainter (*lower panel*) and brighter (*upper panel*) environments. Black and red curves correspond to the 0–0.4 Mpc and 0.4–0.8 Mpc annuli, respectively.

more significant than those defined by fainter galaxies. This result should be related to the well known correlation between galaxy luminosity and clustering amplitude (see for example Zehavi et al. 2005; McCracken et al. 2007; Guo et al. 2013, and references therein). Furthermore, we can reach a number of interesting conclusions regarding the environmental differences between the different source types (AGN, GAL, soft and hard AGN).

For example, X-ray galaxies (GAL sample) are found to be in significantly higher galaxy overdensities when compared to AGN. This can be clearly seen in Fig. 14 where we plot the ratio of the overdensity distributions of the GAL and AGN samples. By large factors (~2–10), the excess of the positive galaxy overdensities around GAL sources compared to those around AGNs can be clearly seen but only in the 0–0.4 Mpc annulus

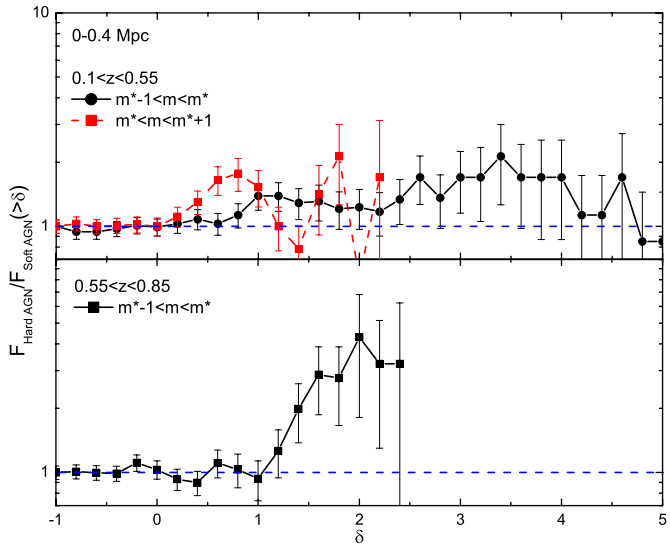

Fig. 15. Ratio of the galaxy overdensity distributions of the hard and soft AGN samples for the 0−0.4 Mpc radial annulus for the fainter (red dashed line) and brighter (black continuous line) environments. *Upper/lower panels* correspond to the lower/higher z-range studied.

(black line) for both fainter and brighter environments. For the latter type of environment, we find that $F(\delta > 0) = 72 \pm 8\%$ (with random expectation 41%) and $F(\delta > 1) = 45 \pm 7\%$. For for comparison, the corresponding values for the AGN sample are $F(\delta > 0) = 63 \pm 5\%$ (with random expectation 43%) and $F(\delta > 1) = 26 \pm 3\%$, respectively.

Unexpected within the unification paradigm, another interesting result is that the soft and hard AGN samples show significant galaxy overdensity distribution differences. Inspecting Fig. 15, where we plot the ratio of the overdensity distributions of the hard and soft AGN samples for those cases where both overdensity distributions are significantly different than their random expectations, we see that the hard AGN sample always has (for $\delta \gtrsim 0$) a higher fraction of higher galaxy overdensity values with respect to the soft AGN's (i.e., $F_{\rm Hard}/F_{\rm Soft}(\delta) > 1$). This is apparent in both redshift ranges, although it appears to be more significant in the higher-z range. This result generally agrees with the correlation function analysis of the XMM-LSS sources by Elyiv et al. (2012), where the clustering of the hard AGNs was found to be stronger than that of the soft AGNs.

Finally, we find another interesting result that is a different redshift evolution of the galaxy overdensity distribution for the soft and hard sources. In the lower panel of Fig. 13, we plot the ratio of the overdensity distributions between the lower and higher redshift ranges separately for the soft (continuous black line) and hard (red dashed line) AGN in the 0−0.4 Mpc radial annulus. There is indication of a systematic difference by which the galaxy overdensities (for $\delta \gtrsim 1.5$) within which the hard AGN are embedded evolve less rapidly than the corresponding overdensities around soft AGN.

5.2. Nearest neighbor statistics

We attempted to investigate the very close environment around each X-ray source by using a nearest neighbor analysis. To this end, we estimated the rest-frame projected linear distance to its nearest optical neighbor (NNb) for each X-ray source using the same CFHTLS galaxy catalog, as in the overdensity analysis, but within the magnitude ranges of $m_{i'}+\Delta m$ with $\Delta m = \pm 0.5$ or ± 1. The parameter $m_{i'}$ is the i'-band magnitude of the host galaxy of the X-ray source. In the current analysis the characteristic magnitude, $m_{i'}$, corresponds to that of the host galaxy. Note that in the overdensity analysis, the characteristic magnitude, m^*, defines the fainter and brighter environment around our X-ray sources and corresponds to the knee of the i-band luminosity function.

Table 5. Kolmogorov-Smirnov probability of the indicated pairs of NNb distributions are drawn from the same parent population and for the indicated magnitude range.

	$\mathcal{P}_{KS}$			
Sample 1/Sample 2	$\Delta m = +1$	$\Delta m = -1$	$\Delta m = 0.5$	$\Delta m = -0.5$
$0.1 \le z \le 0.55$				
All/All$_{\rm rand}$	0.65	0.77	0.98	0.65
GAL/AGN	0.73	0.01	0.55	0.01
Soft AGN/Hard AGN	0.99	0.35	0.55	0.91
$0.55 < z \le 0.85$				
All/All$_{\rm rand}$	0.99	0.73	0.98	0.99
Soft AGN/Hard AGN	0.97	0.99	0.25	0.98

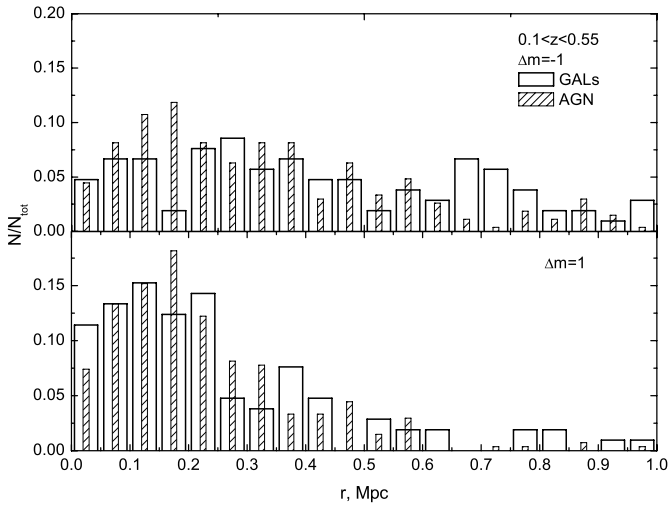

Fig. 16. Differential distributions of the nearest neighbor distance for the GALs and AGN sample for two different magnitude ranges in the $0.1 \le z \le 0.55$ redshift range.

We have then compared the NNb distance distribution of our X-ray sources using the KS two-sampled test to that of randomly selected CFHTLS galaxies having a similar magnitude with that as the X-ray source host ($|m_{i',\text{X-ray}} - m_{i',\text{rand}}| < 0.1$). In this case, we found no significant difference whatsoever. In Table 5, we present the KS probabilities of the indicated pairs of NNb distributions for $\Delta m = +1.0, -1.0, +0.5$, and -0.5, being drawn from the same parent population.

It is evident that the only pair of NNb sample distributions that show a deviation, which are marginally significant ($\mathcal{P}_{KS} \simeq 0.01$) is that of the GAL and AGN brighter neighbors ($\Delta m = -1.0$ and -0.5). Inspecting the two distributions (Fig. 16), we see that the difference is attributed to a deficiency of GAL neighbors at a distance of ∼0.2 Mpc, a corresponding excess at ∼0.7 Mpc, and not to an overall difference in the shape of the distributions. We consider that the observed difference is not very significant and do not discuss it further.

We have also tested the corresponding fifth nearest neighbor distributions, and the results remain the same. We conclude that the NNb analysis applied on our projected data cannot be

effectively used to characterize differences in the very close environment of different types of X-ray sources.

6. Summary and main conclusions

In this paper, we have classified 5142 XMM-LSS X-ray selected sources. To check their reliability and positions, reject problematic objects (i.e. defects in the observations, doubtful counterparts, etc.) and finally classify each object, we visually inspected the optical images of all X-ray counterparts in the g', i' and r' CFHTLS bands. We classified 2441 objects as being extended and 2280 as being point-like, while we rejected from consideration 238 problematic objects and 183 stars (5% and 4% of the whole sample, respectively). We estimated the photometric redshifts of the 4435 objects for which there is available photometry in 4−11 bands [i.e., CFHTLS, *Spitzer*/IRAC, UKIDSS and GALEX] with $i' < 26$ mag. Furthermore, 783 objects also have spectroscopic redshifts. We have found that the photometric redshift accuracy for the objects with available 4−11 band photometry is $\sigma_{\Delta z/(1+z_{\rm sp})} = 0.076$ with $\eta = 22.6\%$ of outliers. The corresponding values for the objects with 7−11 bands are $\sigma_{\Delta z/(1+z_{\rm sp})} = 0.074$ with $\eta = 21.8\%$ and for the subsample of objects with PDZ = 100 are $\sigma_{\Delta z/(1+z_{\rm sp})} = 0.065$ with $\eta = 18.1\%$.

We have considered the multiwavelength properties of 3071 objects that have spectroscopic redshifts or photometric redshifts calculated from 7−11 bands. According to our classification based on spectra, SEDs, and/or $L_{\rm X}$, we have 196 (6.4%) GALs and 2875 (93.6%) AGN/QSOs in our sample. The median HR values in the corresponding quartile ranges for all sources, AGN/QSOs, and GALs are $-0.63^{+0.34}_{-0.37}$, $-0.60^{+0.32}_{-0.40}$, and $-1^{+0.55}_{-0.00}$, respectively. We also have found that 252 objects (8% of our sample) have X/O > 10 and 641 (21%) have $HR \geq -0.2$, which makes them good candidates for obscured AGN/QSOs. We have found 54 DOG candidates (1.7%) in our sample.

We have then defined the environment of 777 X-ray sources (GALs, soft and hard AGN with $HR < -0.2$ and $HR \geq -0.2$, respectively, for which we considered as unobscured and obscured ones) with $-23.5 < M_{i'} < -20$ in the $0.1 \leq z \leq 0.85$ redshift range. The photo-z accuracy for this low redshift sample is $\sigma_{\Delta z/(1+z_{\rm sp})} = 0.061$ with $\eta = 13.8\%$ outliers. Two types of environments have been defined for each X-ray source; an overdensity of fainter and of brighter galaxies (by one magnitude) related to the rest-frame magnitude of the knee of the i'-band luminosity function. Our main results are the following:

(1) *The X-ray point-like sources typically reside in overdense regions, although they can be found even in underdense regions.* We find that ≳55−60% of all X-ray sources are located in overdense environments ($\delta > 0$); this result is significantly higher than the random expectation.

(2) *Overdensities around X-ray sources defined by bright neighbors are significantly higher than those defined by faint neighbors.* For the first redshift range $0.1 \leq z \leq 0.55$, the percentage of objects with positive overdensity having fainter and brighter environments are 58 ± 4% and 66 ± 4% against 45% and 41% expected for the random distribution of the sources, respectively.

(3) *Overdensities around X-ray sources, defined either by brighter or fainter neighbors, are typically higher and more significant in the* $0.1 \leq z \leq 0.55$ *rather than in the* $0.55 < z \leq 0.85$ *redshift range.* Therefore, there appears to be a positive redshift evolution of the galaxy overdensity amplitude within which X-ray sources are embedded.

(4) *X-ray galaxies and AGN inhabit different environments.* X-ray selected galaxies inhabit significantly more overdense brighter galaxy regions in comparison with AGN, indicating possibly that the former prefers more cluster-like environments, while the latter prefers group-like ones. However, the overdensities around X-ray galaxies are significant only up to ∼0.4 Mpc, while those around AGN are significant up to ∼0.8 Mpc. Our results generally agree with Georgakakis et al. (2007, 2008), who showed that X-ray-selected AGN at $z \sim 1$ prefer to reside in groups, and with Bradshaw et al. (2011), who found that X-ray AGN in the UDS (SXDS) field with $1.0 < z < 1.5$ inhabit significantly overdense environments corresponding to dark matter haloes of $M \gtrsim 10^{13} M_{\odot}$.

(5) *The obscured AGN (*$HR \geq -0.2$*) are located in more overdense regions compared to the unobscured AGN (*$HR < -0.2$*).* This is true for both brighter and *fainter* galaxy environments in the $0.1 \leq z \leq 0.55$ redshift range, while it is evident only for the brighter environment in the $0.55 < z \leq 0.85$ range. This result generally agrees with the correlation function analysis of the XMM-LSS X-ray point-source catalog (having a median $z \sim 1$) presented in Elyiv et al. (2012), in which the clustering of the Hard AGN was found to be stronger than that of the soft AGN. Hickox et al. (2011) also found a stronger clustering of obscured QSOs with respect to that of unobscured ones in the $0.7 < z < 1.8$ redshift range in the Bootes multiwavelength survey. Allevato et al. (2011), however, found an opposite trend.

(6) *There are some indications that unobscured AGN (*$HR < -0.2$*) have a more rapid evolution of their galaxy overdensity amplitude,* δ*, between the two redshift ranges studied compared to the obscured AGN (*$HR \geq -0.2$*).*

Acknowledgements. We are grateful to Olivier Ilbert for help with LePhare and to Mari Polletta for useful suggestions. The data used in this work were obtained with *XMM-Newton*, an ESA science mission with instruments and contributions directly funded by ESA Member States and NASA. This work is based on observations obtained with MegaPrime/MegaCam, a joint project of CFHT and CEA/DAPNIA, at the Canada-France-Hawaii Telescope (CFHT), which is operated by the National Research Council (NRC) of Canada, the Institut National des Sciences de l'Univers of the Centre National de la Recherche Scientifique (CNRS) of France, and the University of Hawaii. This work is based in part on data products produced at TERAPIX and the Canadian Astronomy Data Centre as part of the Canada-France-Hawaii Telescope Legacy Survey, a collaborative project of NRC and CNRS. We used the data obtained with the *Spitzer* Space Telescope, which is operated by the Jet Propulsion Laboratory, California Institute of Technology under NASA. Support for this work, part of the *Spitzer* Space Telescope Legacy Science Program, was provided by NASA through an award issued by the Jet Propulsion Laboratory, California Institute of Technology under NASA contract 1407. This work is in part based on data collected within the UKIDSS survey. The UKIDSS project uses the UKIRT Wide Field Camera funded by the UK Particle Physics and Astronomy Research Council (PPARC). Financial resources for WFCAM Science Archive development were provided by the UK Science and Technology Facilities Council (STFC; formerly by PPARC). GALEX is a NASA mission managed by the Jet Propulsion Laboratory. GALEX data used in this paper were obtained from the Multimission Archive at the Space Telescope Science Institute (MAST). STScI is operated by the Association of Universities for Research in Astronomy, Inc. under NASA contract NAS5-26555. Support for MAST for non-HST data is provided by the NASA Office of Space Science via grant NNX09AF08G and by other grants and contracts. This research has made use of the NASA/IPAC Extragalactic Database (NED), which is operated by the Jet Propulsion Laboratory, California Institute of Technology, under contract with the National Aeronautics and Space Administration. O.M., A.E. and J.S. acknowledge support from the ESA PRODEX Programmes "XMM-LSS" and "XXL" and from the Belgian Federal Science Policy Office. They also acknowledge support from the Communauté française de Belgique – Actions de recherche concertées – Académie universitaire Wallonie-Europe.

References

Allevato, V., Finoguenov, A., Cappelluti, N., et al. 2011, ApJ, 736, 99
Antonucci, R. 1993, ARA&A, 31, 473
Arnouts, S., Cristiani, S., Moscardini, L., et al. 1999, MNRAS, 310, 540
Blanton, M. R., Hogg, D. W., Bahcall, N. A., et al. 2003a, ApJ, 594, 186
Blanton, M. R., Hogg, D. W., Bahcall, N. A., et al. 2003b, ApJ, 592, 819
Bradshaw, E. J., Almaini, O., Hartley, W. G., et al. 2011, MNRAS, 415, 2626
Brusa, M., Comastri A., Daddi, E., et al. 2005, A&A, 432, 69
Brusa, M., Fiore, F., Santini, P., et al. 2009, A&A, 507, 1277
Brusa, M., Civano, F., Comastri, A., et al. 2010, ApJ, 716, 348
Brodwin, M., Dey, A., Brown, M. J. I., et al. 2008, ApJ, 687, L65
Burlon, D., Ajello M., Greiner, J., et al. 2011, ApJ, 728, 58
Calzetti, D., Armus, L., Bohlin, R. C., et al. 2000, ApJ, 533, 682
Cardelli, J. A., Clayton, G. C., Mathis, J. S. 1989, ApJ, 345, 245
Chiappetti, L., Tajer, M., Trinchieri, G., et al. 2005, A&A, 439, 413
Chiappetti, L., Clerc, N., Pacaud, F., et al. 2012, MNRAS, submitted
Constantin, A., Hoyle, F., &Vogeley, M. S., 2008, ApJ, 673, 715
Dey, A., Soifer, B. T., Desai, V., et al. 2008, ApJ, 677, 943
Dressler, A. 1980, ApJ, 236, 361
Downes, A. J. B., Peacock, J. A., Savage, A., et al. 1986, MNRAS, 218, 31
Elyiv, A., Clerc, N., & Plionis, M. 2012, A&A, 537, 131
Falder, J. T., Stevens, J. A., Jarvis, M. J., et al. 2010, MNRAS, 405, 347
Fanidakis, N., Baugh, C. M., Benson, A. J., et al. 2012, MNRAS, 419, 2797
Fiore, F., Brusa, M., Cocchia, F., et al. 2003, A&A, 409, 79
Finoguenov, A., Watson, M. G., Tanaka, M., et al. 2010, MNRAS, 403, 2063
Gandhi, P., Crawford, C. S., Fabian, A. C., & Johnstone, R. M. 2004, MNRAS, 348, 529
Gandhi, P., Garcet, O., Disseau, L., et al. 2006, A&A, 457, 393
Garcet, O., Gandhi, P., Gosset, E., et al. 2007, A&A, 474, 473
Geach, J. E., Simpson, C., Rawlings, S., Read, A. M., & Watson, M. 2007, MNRAS, 381, 1369
Georgakakis, A., Nandra, K., Laird, E. S., et al. 2007, ApJ, 660, L15
Georgakakis, A., Gerke, B. F., Nandra, K., et al. 2008, MNRAS, 391, 183
Gilmour, R., Gray, M. E., Almaini, O., et al. 2007, MNRAS, 380, 1467
Guo, H., Zehavi, I., Zheng, Z., et al. 2013, ApJ, 767, 122
Hickox, C., Myers, A. D., Brodwin, M., et al. 2011, ApJ, 731, 117
Hoaglin, D. C., Mosteller, F., & Tukey, J. W. 1983, in Understanding Robust and Exploratory Data Analysis (Wiley Series in Probability and Mathematical Statistics), ed. D. C. Hoaglin, F. Mosteller, & J. W. Tukey (New York: Wiley)
Ilbert, O., Arnouts, S., McCracken, H. J., et al. 2006, A&A, 457, 841
Ilbert, O., Capak, P., Salvato, M., et al. 2009, ApJ, 690, 1236
Kauffmann, G., White, S. D. M., & Heckman, T. M. 2004, MNRAS, 353, 713
Koulouridis, E., Plionis, M., Chavushyan, V., et al. 2006, ApJ, 639, 3745
Koutoulidis, L., Plionis, M., Georgantopoulos, I., & Fanidakis, N. 2013, MNRAS, 428, 1382
Lacy, M., Storrie-Lombardi, L. J., Sajina, A., et al. 2004, ApJSS, 154, 166
Lacy, M., Petric, A. O., Sajina, A., et al. 2007, AJ, 133, 186
Le Fèvre, O., Vettolani, G., Garilli, B., et al. 2005, A&A, 439, 845
Li, C., Kauffmann, G., & Wang, L. 2006, MNRAS, 373, 457
Lietzen, H., Heinamaki, P., Nurmi, P., et al. 2009, A&A, 501, 145
Lietzen, H., Heinamaki, P., Nurmi, P., et al. 2011, A&A, 535, A21
Lidman, C., Ruhlmann-Kleider, V., Sullivan, M., et al. 2012, PASA, accepted
Lupton, R. H., Juric, M., Ivezic, Z., et al. 2005, Bull. AAS, 37, 1384
McCracken, H. J., Peacock, J. A., Guzzo, L., et al. 2007, ApJS, 172, 314
Mignoli, M., Pozzetti, L., Comastri, A., et al. 2004, A&A, 418, 827
Miyaji, T., Krumpe, M., Coil, A. L., & Aceves, H. 2011, ApJ, 726, 83
Montero-Dorta, A. D., Croton, D. J., Renbin, Y., et al. 2009, MNRAS, 392, 125
Nakos, T., Willis, J. P., Andreon, S., et al. 2009, A&A, 494, 579
Ouchi, M., Shimasaku, K., Akiyama, M., et al. 2008, ApJS, 176, 301
Pierre, M., Chiappetti, L., Pacaud, F., et al. 2007, MNRAS, 382, 279
Poggianti, B. 1997, A&AS, 122, 399
Polletta, M., Tajer, M., Maraschi, L., et al. 2007, ApJ, 663, 81
Prevot, M. L., Lequeux, J., Prevot, L., et al. 1984, A&A, 132, 389
Schawinski, K., Virani, S., Simmons, B., et al. 2009, ApJ, 692, L19
Schlegel, D. J., Finkbeiner, D. P., & Davis, M. 1998, ApJ, 500, 525
Salvato, M., Hasinger, G., Ilbert, O., et al. 2009, ApJ, 690, 1250
Salvato, M., Ilbert, O., Hasinger, G., et al. 2011, ApJ, 742, 61
Silverman, J. D., Kovac, K., Knobel, C., et al. 2009, ApJ, 695, 171
Simpson, C., Martinez-Sansigre A., Rawlings, S., et al. 2006, MNRAS, 372, 741
Simpson, C., Rawlings, S., Ivison, R., et al. 2012, MNRAS, 421, 2012
Smail, I., Sharp, R., Swinbank, A. M., et al. 2008, MNRAS, 389, 407
Sorrentino, G., Radovich, M., & Rifatto, A. 2006, A&A, 451, 809
Stalin, C. S., Petitjean, P., Srianand, R., et al. 2010, MNRAS, 401, 294
Stern, D., Eisenhardt, P., Gorjian, V., et al. 2005, ApJ, 631, 163
Strand, N. E., Brunner, R. J., & Myers, A. D. 2008, ApJ, 688, 180
Tajer, M., Polletta, M., Chiappetti, L., et al. 2007, A&A, 467, 73
Tasse, C., Le Borgne, D., Rottgering, H., et al. 2008a, A&A, 490, 879
Tasse, C., Best, P. N., Rottgering, H., & Le Borgne, D. 2008b, A&A, 490, 893
Tasse, C., Rottgering, H., & Best P. N. 2011, A&A, 525, A127
van Breukelen, C., Cotter, G., Rawlings, S., et al. 2007, MNRAS, 382, 971
van Breukelen, C., Simpson, C., Rawlings, S., et al. 2009, MNRAS, 395, 11
van der Wel, A. 2008, ApJ, 675, L13
Warren, S. J., Hewett, P. C., & Osmer, P. S. 1994, ApJ, 421, 412
Waskett, T. J., Eales, S. A., Gear, W. K., et al. 2005, MNRAS, 363, 801
Ueda, Y., Watson, M. G., Stewart, I. M., et al. 2008, ApJS, 179, 124
Zehavi, I., Zheng, Z., Weinberg, D. H., et al. 2005, ApJ, 630, 1